

# Testing new chromophores for singlet fission: a computational protocol applied to 2,3-diamino-1,4-benzoquinone.

Davide Accomasso<sup>a</sup>, Giovanni Granucci<sup>a</sup>, Remco W. A. Havenith<sup>b,c</sup>,  
Maurizio Persico<sup>a</sup>

<sup>a</sup> Università di Pisa, Dipartimento di Chimica e Chimica Industriale,  
via Moruzzi 13, 56124 Pisa, Italy

<sup>b</sup> Theoretical Chemistry, Zernike Institute for Advanced Materials  
and Stratingh Institute for Chemistry, University of Groningen,  
Nijenborgh 4, 9747 AG Groningen, The Netherlands

<sup>c</sup> Ghent Quantum Chemistry Group, Department of Inorganic and Physical Chemistry,  
Ghent University, Krijgslaan 281 (S3) B-9000 Gent, Belgium

**Abstract:** We present a computational protocol devised to test the suitability of newly proposed chromophores for singlet fission. The protocol includes two main steps: testing the basic energetic requirements by ab initio calculations and simulating the photodynamics to determine singlet fission quantum yields. We applied this protocol to 2,3-diamino-1,4-benzoquinone (DAPBQ), recently proposed as a possible chromophore for singlet fission. We determined the excitation energies of DAPBQ by second order perturbation CASPT2 and NEVPT2 calculations. Then, we optimized a possible crystal structure of DAPBQ, we identified the most favourable pair of molecules within it and we ran a simulation of the excited state dynamics for that dimer embedded in the crystal at a semiempirical QM/MM level. The results indicate that DAPBQ in the crystalline phase does not undergo singlet fission and the initially prepared singlet excited state rapidly decays to the ground state.

## 1. Introduction

Singlet fission is a process in which a chromophore A in an excited singlet state ( $S_1$ ) transfers part of its excitation energy to a neighbouring chromophore B in the ground state ( $S_0$ ) and both are converted into triplet excited states ( $T_1$ ) [1, 2]:



This process can be exploited to improve the efficiency of photovoltaic devices. In fact, a sensitizer capable of quantitative singlet fission may generate two charge carrier pairs per absorbed photon in the conduction band of a semiconductor material. In 2006 it was shown [3] that singlet fission can raise the maximum power conversion efficiency of single-junction photovoltaic devices from the Shockley-Queisser limit [4] of 33.7% to 44.4%.

In the molecular pair (hereafter called the dimer) the two triplets generated via singlet fission can combine into a pure singlet state, the  $^1(T_1T_1)$  state, so the total spin can be conserved and the process is spin-allowed. Like many other spin-allowed processes, singlet fission is potentially fast and can occur on a sub-picosecond time scale [5, 6].

To occur with a high yield, singlet fission must be energetically favored. For two identical chromophores ( $B=A$ ) weakly interacting, this leads to the following energy condition:

$$\Delta E(S_1) \geq 2 \Delta E(T_1) \quad (2)$$

Moreover, once Equation (2) is fulfilled, it is desirable to reduce as much as possible the triplet-triplet annihilation  $A(T_1) + B(T_1) \rightarrow A(T_2) + B(S_0)$ . This yields to the second energy condition:

$$\Delta E(T_2) > 2 \Delta E(T_1) \quad (3)$$

In Equations (2) and (3), the energies  $\Delta E(S_1)$ ,  $\Delta E(T_1)$  and  $\Delta E(T_2)$  are all differences with respect to the ground state  $S_0$ . If the singlet fission is ultrafast, in principle it is sufficient to satisfy a “weak” version of the first requirement, Equation (2), where  $\Delta E(S_1)$  is the vertical transition energy and  $\Delta E(T_1)$  is the adiabatic one. However, if the thermal equilibration of the excited chromophore is faster than the singlet fission, one must compare the adiabatic transition energies, which corresponds to a “strong” version of the inequality (2). The second requirement, Equation (3), clearly involves adiabatic transition energies. Moreover, for photovoltaic applications the triplet adiabatic energy  $\Delta E(T_1)$  must exceed the band gap of the semiconductor in use.

In this work we present a thorough analysis of the suitability of a newly proposed chromophore for singlet fission. We first determine the vertical and adiabatic transition energies of  $S_1$  and  $T_1$  by accurate ab initio methods, to verify whether the condition (2) is satisfied. Even if the first test is positive, the singlet fission quantum yield may be too low, because of the competition with other processes such as Internal Conversion or InterSystem Crossing in a single chromophore. To determine the quantum yields we run a computational simulation of the photodynamics for the dimer. In this work we deal with a molecular crystal, the structure of which must be determined. Then, the most favorable pair of adjacent monomers within the crystal is identified as the one with the strongest interaction between the  $S_1$  and  ${}^1(T_1T_1)$  states. For the simulation of the photodynamics we adopt the Surface Hopping method [7] and a QM/MM scheme [8], where the QM subsystem is the chosen dimer and the MM subsystem is the rest of the crystal.

This procedure, or variants of it, can be used to sort out chromophores that fulfill the energetic requirements and undergo singlet fission with acceptable quantum yields. Once a viable chromophore has been identified, the same analysis can be applied to improve its design, by testing the effectiveness of structural variants, of mutual orientations of the two monomers and of different embeddings.

So far, two main classes of likely singlet fission systems have been identified: (i) large even alternant hydrocarbons (such as anthracene [9], tetracene [10] and pentacene [6]) and (ii) biradicaloids [11–14]. In the present work, the system under investigation is the 2,3-diamino-1,4-benzoquinone (DAPBQ) (Figure 1), that belongs to the class of captodatively stabilized biradicaloids. According to the ab initio calculations performed by Wen et al. [14], it satisfies the desired adiabatic energy criteria, Equations (2) and (3). In this work, we carried out CASPT2 and NEVPT2 calculations to further inspect the excitation energies of DAPBQ (see Section 2). In the same section we also present the crystal structure of DAPBQ, computed at DFT level. Subsequently, in Section 3 we describe the QM/MM simulation of excited state dynamics for a dimer of DAPBQ in the crystal, using a trajectory surface hopping approach.

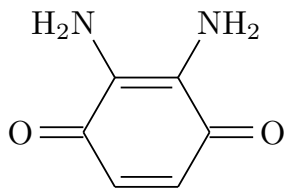


Figure 1: Molecular structure of 2,3-diamino-1,4-benzoquinone (DAPBQ).

## 2. Ab initio calculations on DAPBQ

The vertical and adiabatic excitation energies for the low-lying electronic states of DAPBQ were calculated using the second order perturbation methods CASPT2 [15, 16] and NEVPT2 [17–19], with the ANO-L-VTZP [20, 21] basis set. In all calculations  $C_2$  symmetry was used. The CASSCF reference energies and wavefunctions were obtained in a state-specific manner, using an active space of 12 electrons and 12 orbitals (8  $\pi$  and 4  $\sigma$  orbitals). In the second order perturbation calculations all orbitals except the 1s cores were correlated. Ground and excited state geometries were optimized at the CASPT2/ANO-L-VTZP level of theory. All CASPT2 calculations were performed using an IPEA shift [22] of 0.25 a.u. and the MOLCAS 8.0 [23] program package. Since the CASPT2 analytical gradients are not available in MOLCAS 8.0, the geometry optimizations were run numerically. The NEVPT2 calculations were performed at the CASPT2 optimized geometries in two variants, the partially contracted (PC) and the strongly contracted (SC) scheme [17], using the MOLPRO [24] program package.

The CASPT2 optimized geometries are reported in the Supporting Information (Section S2). The natural orbitals of the active space for  $S_0$  at the optimized geometry are shown in Figure S3. They are very similar to the active orbitals for  $S_0$  of 2,3-dichloro-1,4-benzoquinone (Figure S2), obtained in the benchmark calculations (see Section S1) and they do not differ qualitatively from the active orbitals for  $S_1$  and  $T_1$ . The first singlet and triplet excited states of DAPBQ are mainly  $\pi \rightarrow \pi^*$  excitations with a significant charge transfer character. A schematic representation of the dominant electron promotions in these two states is provided in Figure 2. In Table 1 we show the vertical and adiabatic excitation energies obtained at CASSCF, CASPT2, PC- and SC-NEVPT2 level.

From the CASPT2 results it appears that the first adiabatic energy condition for singlet fission, Equation (2), is not fulfilled. This is in disagreement with the results of Wen et al., who used a smaller basis set (ANO-S-VDZP) for geometry optimizations and a smaller active space (12 electrons and 10 orbitals) [14]. In particular, the CASPT2 excitation energies of  $S_1$  obtained in the present work (vertical 2.44 eV, adiabatic 1.68 eV, see Table 1) are significantly lower with respect to the values reported in Ref. [14] (2.63 and 2.23 eV). Even when a systematic error of 0.3 eV is assumed for the adiabatic excitation energy of  $S_1$ , as discussed in the Supporting Information (Section S1.3), the condition of Equation (2) is not satisfied by 0.5 eV.

At the PC-NEVPT2 level, while the excitation energies of  $T_1$  (vertical 1.87 eV, adiabatic 1.23 eV, see Table 1) are in excellent agreement with the CASPT2 results, the energies for  $S_1$  are even lower (by about 0.1 eV). Moreover, the energies obtained using the SC-NEVPT2 method, which might be considered more approximate than the PC version, do not differ significantly from the CASPT2 results. Thus, the NEVPT2 energies confirm that the “strong” version of the energy condition (2) is not satisfied.

It is worth noting that in our calculations, as well as in those performed by Wen et al. [14], the CASPT2 corrections on the CASSCF relative energies are quite large, especially for  $S_1$ , making the CASPT2 results more uncertain. However, the excitation energies computed using the NEVPT2 method, which is generally considered more accurate than CASPT2, are in good agreement with the CASPT2 ones.

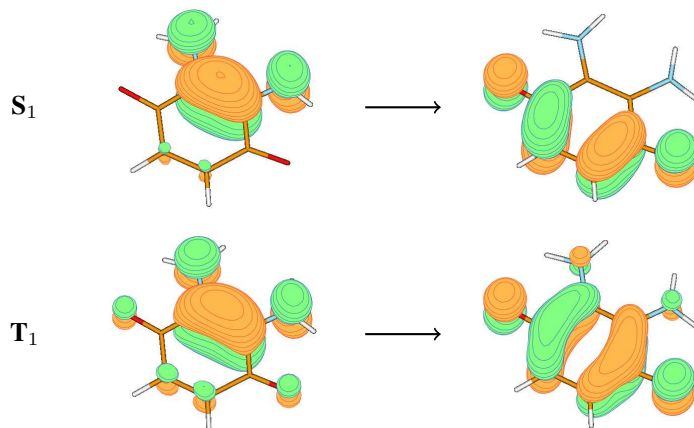


Figure 2: Dominant electron promotions in the  $S_1$  and  $T_1$  states of DAPBQ. Natural orbitals of the active space for  $S_1$  and  $T_1$  at their equilibrium geometries are shown.

Table 1: CASSCF, CASPT2, PC- and SC-NEVPT2/ANO-L-VTZP excitation energies (in eV) of the  $S_1$  and  $T_1$  electronic states evaluated at CASPT2/ANO-L-VTZP optimized geometries for DAPBQ. The  $C_2$  symmetry was used. The CASSCF, CASPT2, PC- and SC-NEVPT2 energies of  $S_0$  are -489.70801, -491.28270, -491.26360 and -491.25480 a.u., respectively.

Method	State	Label	Geometry		
			$S_0$ min.	$S_1$ min.	$T_1$ min.
CASSCF	$S_0$	$1^1A$	0.00	1.01	0.85
	$S_1$	$1^1B$	4.14	3.36	3.41
	$T_1$	$1^3B$	2.73	2.60	2.46
CASPT2	$S_0$	$1^1A$	0.00	0.75	0.61
	$S_1$	$1^1B$	2.44	1.68	1.72
	$T_1$	$1^3B$	1.86	1.27	1.24
PC-NEVPT2	$S_0$	$1^1A$	0.00	0.75	0.61
	$S_1$	$1^1B$	2.34	1.53	1.58
	$T_1$	$1^3B$	1.87	1.25	1.23
SC-NEVPT2	$S_0$	$1^1A$	0.00	0.73	0.59
	$S_1$	$1^1B$	2.49	1.62	1.68
	$T_1$	$1^3B$	1.95	1.30	1.27

To determine a possible crystal structure for DAPBQ, which is not known experimentally, periodic DFT calculations were performed starting from the known crystal structure of 2,3-dimethyl-1,4-benzoquinone [25]. We ended up with a structure of  $P_1$  symmetry,

which is a minimum (no imaginary frequencies), with optimized cell parameters and structure shown in Table 2 and Figure 3. The unit cell atomic coordinates of the computed crystal structure are reported in the Supporting Information (Section S3).

All periodic DFT calculations were carried out with the Crystal14 code [26], using the B3LYP functional with the Grimme dispersion correction [27] and the 6-21G basis set. A grid of  $8 \times 8 \times 8$  k points in the reciprocal space, according to Pack-Monkhorst method [28], was used. In the calculations not only the atomic positions, but also the cell parameters were optimized.

Table 2: Information about the calculated crystal structure of DAPBQ.

Space group	Lattice parameters (angstroms and degrees)						Density (g/cm <sup>3</sup> )	Unit cell energy (a.u)
	a	b	c	$\alpha$	$\beta$	$\gamma$		
P <sub>1</sub>	10.208	4.957	10.208	96.18	93.25	84.21	1.797	-1965.64719

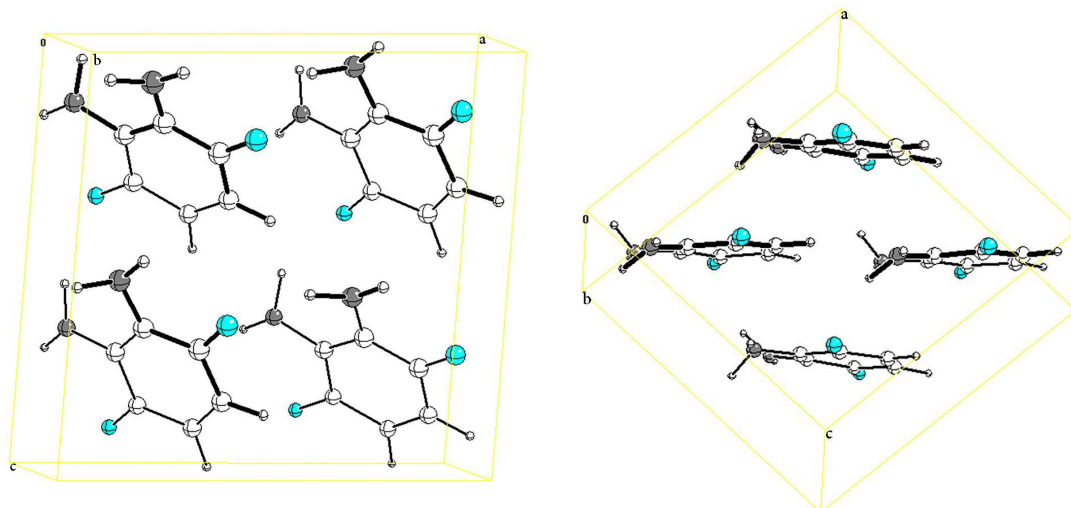


Figure 3: Unit cell of the computed crystal structure of DAPBQ. Two different views are shown.

### 3. QM/MM simulation of excited state dynamics

As shown in the preceding section, probably DAPBQ does not satisfy the energetic criterion for singlet fission. However, in view of previous results [14] at variance with ours, and considering that small modifications of the DAPBQ structure might improve its energetics, we decided to simulate the excited state dynamics of a dimer of DAPBQ in a crystalline environment.

In the simulation, we follow a quantum mechanical/molecular mechanical type (QM/MM) approach, in which two neighbouring molecules of the crystal structure are treated quantum-mechanically, while the rest of the crystal is described at the molecular mechanics level. The interaction between the QM and MM subsystems is treated using the electrostatic embedding scheme [8].

### 3.1. Parameters choice

To treat the QM dimer, the FOMO-CI [7, 29] method with the PM3 [30] semiempirical Hamiltonian and a CAS-CI active space of 12 electrons in 8 orbitals were selected. The floating occupation numbers were determined using a gaussian energy width of 0.1 a.u. By default, in the FOMO method only the active MO's have fractional occupations. However, in the dynamics simulations, at some geometries we found convergence problems of the SCF procedure, that were partially overcome by adding four occupied MO's to the orbitals with floating occupation numbers, keeping the active space of 12 electrons in 8 orbitals for the CAS-CI calculation.

The vertical and adiabatic excitation energies for the  $S_1$  and  $T_1$  electronic states of the monomer obtained at this level of theory (using an active space of 6 electrons in 4 orbitals) are in good agreement with the CASPT2 results reported in Ref. [14] (see Table S6). At the considered geometries (minima of  $S_0$ ,  $S_1$  and  $T_1$ ) one lone pair orbital of the oxygen atoms and three  $\pi$  orbitals are active (Figure S4). Moreover, in line with the CASPT2 and NEVPT2 results,  $S_1$  and  $T_1$  are reasonably described as HOMO  $\rightarrow$  LUMO  $\pi \rightarrow \pi^*$  electron promotions.

For the MM subsystem we used the OPLS-AA force field [31], as implemented in the TINKER 6.3 [32] molecular modeling package. For each atom of the DAPBQ molecule an appropriate atom type was selected (see Table S7). Moreover, the atomic charges, reported in Table S8, were determined at the CAM-B3LYP/TZVP level using the CHELPG (CHarges from ELectrostatic Potentials using a Grid based method) scheme [33] with the additional constraint of reproducing the overall molecular dipole moment.

To test the force field, we performed a geometry optimization on one molecule at the MM level, using  $C_2$  symmetry. The geometry obtained is in good agreement with the CASPT2/ANO-L-VTZP optimized ground state geometry (see Table S9).

### 3.2. Preparation of the system for the QM/MM simulation

Starting from the crystal structure obtained at the B3LYP-D/6-21G level, an MM optimization of the atomic positions in the unit cell, using periodic boundary conditions, was performed. Then, using the MM optimized crystal structure as input geometry, a molecular dynamics trajectory in a constant temperature mode, using the Berendsen thermostat algorithm, was carried out. In the dynamics a temperature of 300 K, a time step of 1 femtosecond and a total time of 10 nanoseconds were used. Moreover, periodic boundary conditions were imposed on the unit cell. The crystal structure optimization and the thermal equilibration at the molecular mechanics level were performed using the TINKER 6.3 [32] molecular modeling package.

The cluster for the QM/MM simulations was constructed by replicating a single unit cell 3 times along the a and c crystalline axes and 7 times along the b axis. In this way an approximately cubic cluster was obtained. The "cube" contains 512 molecules (8 molecules along each edge, Figure 4). In the dynamics two neighbouring molecules in the bulk of the system were treated at the semiempirical level, while the other molecules were described using the OPLS-AA force field (Figure 4). In order to keep the overall crystal structure, all molecules in the 6 faces of the irregular cube were frozen during the simulation.

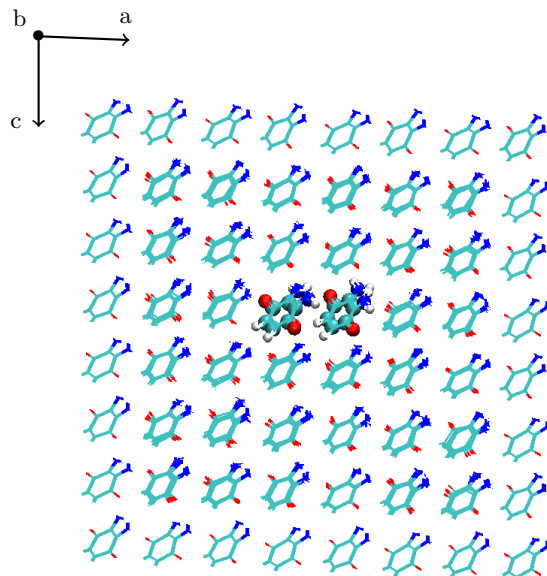


Figure 4: The approximately cubic cluster for the QM/MM simulation. The QM dimer is represented with ball atoms and stick bonds, while the MM molecules are shown in simple line drawing. A different view is shown in the Supporting Information (Figure S10).

### 3.3. Selection of the QM dimer

In the crystal structure computed at the DFT level (Section 2) the 15 different pairs of neighbouring molecules were identified (see Section S5). In the attempt to select the dimer with the most favourable interchromophore electronic coupling for singlet fission, the following strategy was used:

- for each of the 15 dimers a single-point QM/MM calculation is performed, using the approximately cubic cluster described in Section 3.2
- the transition dipole moment  $\langle S_0S_0 | \hat{\mu} | {}^1(T_1T_1) \rangle$  between the ground state  $S_0S_0$  and the singlet combination of the two triplets state  ${}^1(T_1T_1)$  is calculated
- the pair of molecules with the highest absolute value of  $\langle S_0S_0 | \hat{\mu} | {}^1(T_1T_1) \rangle$  is selected.

This choice is based on the assumption that the dipole strength of the  $S_0S_0 \rightarrow {}^1(T_1T_1)$  transition is a good measure of the interaction between the  ${}^1(T_1T_1)$  state and the monomer singlet states. In fact, without the contribution of the monomer singlets, the transition dipole moment for the pure  ${}^1(T_1T_1)$  state is zero, because the one-electron density matrix connecting  $S_0S_0$  and  ${}^1(T_1T_1)$  vanishes (see Ref. [34]). The largest contributions are those of the  $S_1S_0$  and  $S_0S_1$  states that are involved in the singlet fission, because they are the closest in energy to  ${}^1(T_1T_1)$  and have large transition dipoles with the ground state. The absolute values of  $\langle S_0S_0 | \hat{\mu} | {}^1(T_1T_1) \rangle$  for the different dimers are reported in Table S10. The highest value is associated to the QM/MM dimer shown in Figure 4.

### 3.4. QM/MM simulation

The QM/MM simulation of the excited state dynamics was performed using a semi-classical trajectory surface hopping approach with “on the fly” semiempirical QM/MM

calculation of energies and wavefunctions (DTSH method) [7, 8]. The overlap decoherence correction scheme [35] was used to take into account the quantum decoherence effect in a surface hopping framework. The calculations were carried out with a development version of the MOPAC code [36] in which the DTSH dynamics and the QM/MM FOMO-CI electronic structure method were implemented.

The 5 lowest electronic singlet states of the dimer (the QM part) were included in the simulation. They are the ground state, two excited states that can reasonably be described as electron promotions  $h_A \rightarrow l_A$  and  $h_B \rightarrow l_B$  (Figure 5) or their linear combinations, the singlet combination of the two triplets state, which is mainly a double excitation  $h_A, h_B \rightarrow l_A, l_B$ , and a charge-transfer state, which corresponds to a mixture of  $h_A \rightarrow l_B$  and  $h_B \rightarrow l_A$  transitions, where an electron is transferred from one QM molecule to the other (here with  $h_X$  and  $l_X$  we indicate the HOMO and LUMO orbitals of monomer  $X$ , respectively).

A ground state thermal equilibration of the QM/MM system using the Bussi-Parrinello stochastic thermostat [37] was then performed, with a temperature of 300 K, a time step of 0.1 femtoseconds and a total time of 50 picoseconds. The initial nuclear coordinates and momenta were taken from a snapshot of the thermalized MM trajectory (Section 3.2). The spectrum obtained from the QM/MM thermal equilibration on the ground state is shown in Figure S11. Among the five lowest in energy electronic singlet states of the system,  $S_2$  shows the highest extinction coefficient, followed by  $S_1$ . The large difference between the strength of the  $S_1$  and  $S_2$  overlapping bands shows the importance of excitonic mixing. The other two transitions,  $S_0 \rightarrow S_3$  and  $S_0 \rightarrow S_4$ , which correspond to the  $^1(T_1T_1)$  and charge transfer states, show very low extinction coefficients.

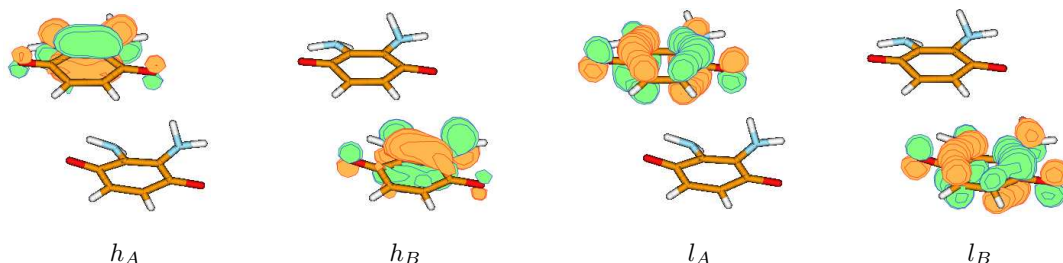


Figure 5: Frontier molecular orbitals of the dimer.

Initial conditions (the initial electronic state, nuclear coordinates and velocities) for 214 excited state trajectories were sampled from the phase space distribution generated in the thermal equilibration. The sampling was performed as described in [38, 39]. Each state is selected according to its excitation probability which is proportional to the square of the transition dipole moment. In the sampling procedure, a transition energy window between 2 and 3.2 eV was used; this energy interval includes the entire strong band of the spectrum shown in Figure S11. Each trajectory was stopped if both the following conditions were satisfied for a time interval of 100 femtoseconds: the trajectory is on the ground state and the energy difference with the first excited state is higher than 0.01 a.u. ( $\sim 0.3$  eV).

Figure 6 shows the fractions of trajectories (populations) of the electronic states included in the simulation as functions of time. As can be seen, the decay of  $S_2$  and  $S_3$  to the lowest excited state ( $S_1$ ) is very fast. After being populated by internal conversion, the  $S_1$  state decays rapidly to the ground state ( $S_0$ ). The population of  $S_0$  can be fitted by a

single exponential function  $1 - e^{-t/\tau}$ , with  $\tau \simeq 700$  fs (Figure 6). Starting from a singly excited state, the  $^1(T_1T_1)$  state is not populated before the decay of  $S_1$  to  $S_0$  occurs. However, our simulations indicate that, once populated, the  $^1(T_1T_1)$  state is stable. In fact, one trajectory out of 214 started in a state which is mainly  $^1(T_1T_1)$  with contributions from charge-transfer configurations. In this case, the decay of the initial state to  $S_0$  did not occur and the trajectory propagated on the  $^1(T_1T_1)$  state for the entire simulation time (10 ps).

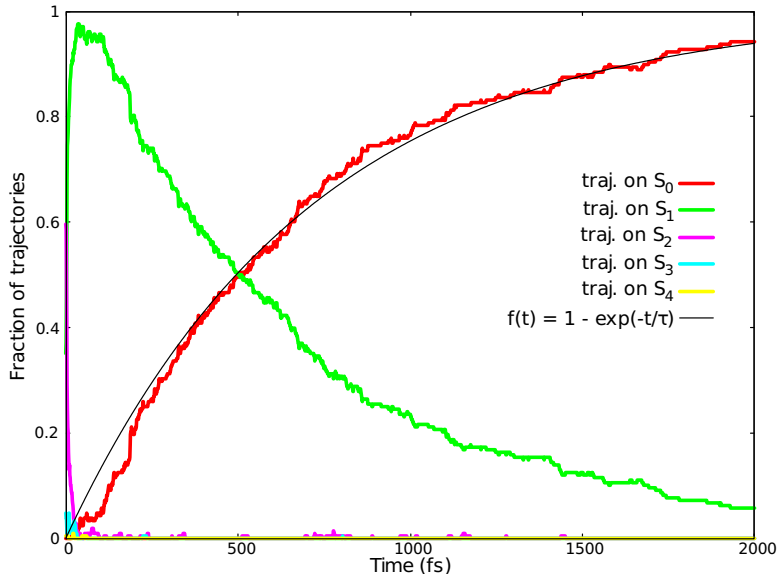


Figure 6: Fraction of trajectories on the five singlet states included in the QM/MM simulation as function of time. The red curve is fitted by an exponential function  $1 - e^{-t/\tau}$ , with  $\tau \simeq 700$  fs.

To understand whether the fast deactivation of the excited state is typical of the isolated chromophore or is caused by the interaction with the crystalline environment, the simulation of excited state dynamics for an isolated DAPBQ molecule was carried out. After a thermal equilibration on the ground state at the temperature of 300 K using the Bussi-Parrinello stochastic thermostat [37], 208 initial conditions were sampled with the procedure described in [38, 39]. Only the  $S_1$  and  $S_0$  states were included in the dynamics. Their populations as functions of time are shown in Figure S12. The decay of  $S_1$  to  $S_0$  is much slower than in the QM/MM dimer; in fact, the population of  $S_0$  can be fitted by the function  $1 - e^{-t/\tau}$ , with  $\tau \simeq 25$  ps. Thus, the fast deactivation of the excited state in the crystal appears to be due to the interaction of the initially excited QM molecule with the surrounding ones.

Since in the computed crystal structure of DAPBQ the molecules are hydrogen bonded, an excited state deactivation induced by hydrogen bonding or even proton transfer may explain the fast excited state decay found in the simulation. In fact, the initial state, mainly a single excitation localized on one molecule, has a significant charge-transfer character: electron density is transferred from the amino (donor) to the carbonyl (acceptor) groups, which acquire a partial negative charge. The interactions between the oxygen atoms of the initially excited molecule and the hydrogens of the neighbouring molecules are therefore even more stabilizing than in the ground state. They may lower the excited state energy,

making the  $S_1$ - $S_0$  energy gap very small and the internal conversion from  $S_1$  to  $S_0$  much faster.

To test this hypothesis, QM/MM calculations on a QM DAPBQ molecule interacting with one or two MM hydrogen atoms were performed. The QM part was treated as the isolated monomer (see Section 3.1). For the MM part, the parameters for the amine hydrogens were employed (see Tables S7 and S8), as in the dynamics. Starting from the geometry shown in Figure 7a, where the QM molecule is at the equilibrium geometry of  $S_1$  and the MM hydrogen is positioned so as to reproduce the hydrogen bond orientation in the crystal structure (Figure 8), the distance between the MM hydrogen and the QM oxygen was varied, while the other internal coordinates of the system were fixed. At each value of the OH distance considered, the  $S_1$ - $S_0$  energy gap was computed. As the OH distance decreases, the energy difference between  $S_1$  and  $S_0$  becomes smaller (Figure 7, red line). If a second MM hydrogen atom is included, as illustrated in Figure 7b, and both OH distances are varied and set to the same value in each single point calculation, the effect is much stronger (Figure 7, green line). Starting from an energy difference of about 1 eV for  $R(\text{OH}) = 3 \text{ \AA}$ , when both OH distances are set to a value of  $1 \text{ \AA}$  the  $S_1$  and  $S_0$  states are nearly degenerate.

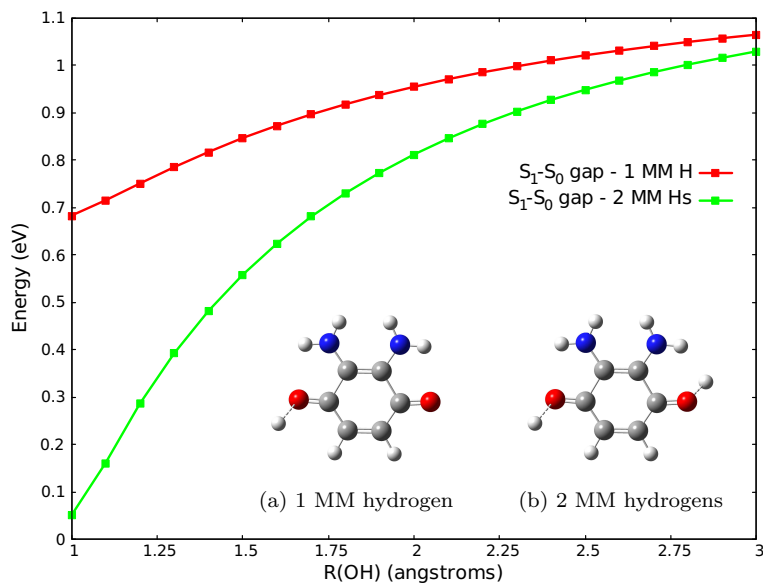


Figure 7:  $S_1$ - $S_0$  energy gap as function of the hydrogen bond length shown in Figure (a) (red line) and of the two OH distances shown in Figure (b) (green line).

One more evidence of the role of the hydrogen bonding in the excited state decay is the correlation between the shortening of  $\text{N-H} \cdots \text{O}$  hydrogen bonds and the occurrence of surface hops. In the QM dimer, atom O1 of molecule A can form a hydrogen bond with atom H29 or H30 of molecule B (Figure 8). We considered the shortest of these two intermolecular OH distances,  $R(\text{OH})$ , and we computed its mean value for the initial conditions ( $t = 0$ ) of the 214 surface hopping trajectories, which is  $\langle R(\text{OH}) \rangle = 2.35 \text{ \AA}$  with a standard deviation of  $0.43 \text{ \AA}$ . Figure 9 shows the values of  $R(\text{OH})$  and the corresponding  $S_1$ - $S_0$  energy gaps at the geometries of the  $S_1 \rightarrow S_0$  hops. The  $R(\text{OH})$  distances tend to be considerably shorter than the initial ones, especially for the hops

taking place when the excitation is localized on molecule A, which is the hydrogen bond acceptor (red dots in the plot). By restricting the average to the red dots,  $\langle R(\text{OH}) \rangle = 2.07 \pm 0.35$  is obtained, i.e. the distribution of the  $R(\text{OH})$  values is shifted by  $-0.28$  Å. Quite similar results are obtained by considering the molecules B (QM) and C (MM) in Figure 8. An intermolecular hydrogen bond can be formed between atom O17 and H45 or H46, at the QM/MM boundary. Taking as before the shortest of these two OH distances, at  $t = 0$  the average is  $\langle R(\text{OH}) \rangle = 2.01 \pm 0.26$  Å. Figure 9 again shows that  $R(\text{OH})$  tends to be shorter at the time of surface hops and the effect is more evident when the excitation is localized on molecule B, which is in this case the hydrogen bond acceptor (green dots). The average for the green dots is  $\langle R(\text{OH}) \rangle = 1.75 \pm 0.17$  Å, with a shift of  $-0.26$  Å. Although the N-H $\cdots$ O hydrogen bond between an MM molecule and a QM one is considerably shorter than that between two QM molecules, both appear to accelerate the decay of the  $S_1$  state by decreasing the  $S_1$ - $S_0$  energy gap.

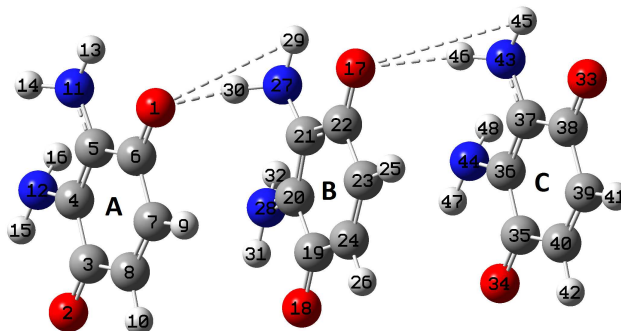


Figure 8: Molecules extracted from the crystal structure. Molecules A and B form the QM subsystem, while molecule C belongs to the MM environment.

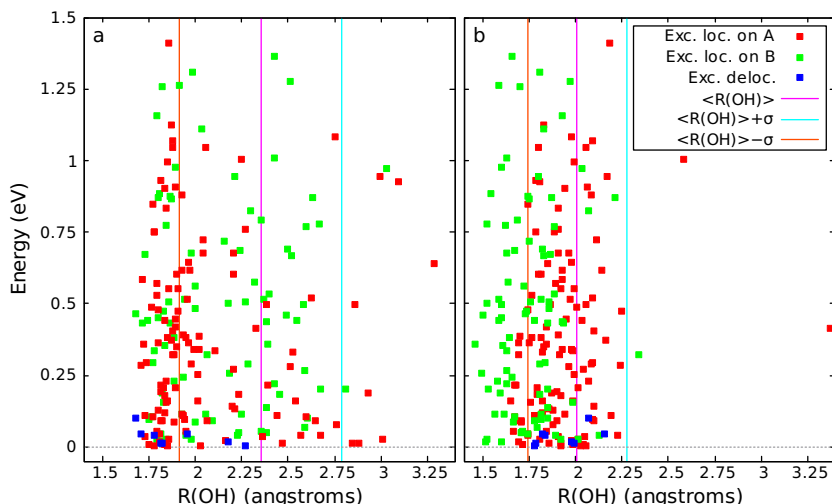


Figure 9: The  $S_1$ - $S_0$  energy gap versus the  $R(\text{OH})$  distance at the time of surface hops. Panel a:  $R(\text{OH})$  is the shortest of the O1-H29 and O1-H30 distances. Panel b:  $R(\text{OH})$  is the shortest of the O17-H45 and O17-H46 distances. For comparison,  $\langle R(\text{OH}) \rangle$  and  $\sigma$  are also shown, i.e. respectively the mean value and the standard deviation of  $R(\text{OH})$  at the beginning of the trajectories.

Combining these findings with the results reported in Figure 7, we conclude that in the excited state the molecule on which the excitation is localized tends to form stronger hydrogen bonds with the surrounding molecules than in the ground state; these interactions lead to a significant decrease of the energy difference between  $S_1$  and  $S_0$  and hence to a faster decay of the excited state.

#### 4. Conclusions

We performed a full computational investigation of 2,3-diamino-1,4-benzoquinone (DAPBQ) as a candidate chromophore for singlet fission. Our study provides a complete overview of the steps needed to test the efficiency of singlet fission in a hitherto unknown molecule. It includes preliminary CASPT2 and NEVPT2 calculations, the determination of a plausible crystal structure for this molecule, the individuation of the pair of nearest neighbours with the largest coupling between the electronic states involved in singlet fission, and a full simulation of the nonadiabatic dynamics within the crystal by the surface hopping method.

Our CASPT2 and NEVPT2 calculations indicated that, in contrast with the results of Wen et al. [14], DAPBQ does not satisfy the basic energetic criterion for singlet fission. However, the vertical excitation energy to  $S_1$  is only slightly less than twice the adiabatic energy of  $T_1$ , so photon absorption in the short wavelength side of the  $S_0 \rightarrow S_1$  band might still provide enough energy to generate two triplet states. Moreover, even discounting the unavoidable uncertainty of the quantum chemical results, small modifications of the DAPBQ structure or of its environment might lead to more favourable energetics. Therefore, we also simulated the excited state dynamics of a dimer of DAPBQ in a crystalline environment, using the more encouraging excitation energies of  $S_1$  and  $T_1$  computed by Wen et al. [14] as reference values.

The outcome of the QM/MM simulation showed that in the crystalline DAPBQ fast decay to the ground state outcompetes singlet fission. Specifically, in the excited state the strengthening of the N-H $\cdots$ O intermolecular hydrogen bonds with respect to the ground state leads to a significant decrease of the energy difference between  $S_1$  and  $S_0$  and hence to a very fast decay of the excited state. Structural modifications of DAPBQ aimed at designing a better candidate for singlet fission should therefore prevent the formation of N-H $\cdots$ O hydrogen bonds, as well as increase slightly the difference between the  $T_1$  and  $S_1$  excitation energies.

#### Acknowledgements

We thank Ria Broer and Josef Michl for enlightening discussions. This work was financially supported by the University of Pisa. One of us (D.A.) is grateful to the Erasmus Placement program for supporting his stay at the University of Groningen.

- [1] M. B. Smith and J. Michl. Singlet fission. *Chem. Rev.*, 110:6891–6936, 2010.
- [2] M. B. Smith and J. Michl. Recent advances in singlet fission. *Annu. Rev. Phys. Chem.*, 64:361–386, 2013.

- [3] M. C. Hanna and A. J. Nozik. Solar conversion efficiency of photovoltaic and photoelectrolysis cells with carrier multiplication absorbers. *J. Appl. Phys.*, 100:074510/1–074510/8, 2006.
- [4] W. Shockley and H. J. Queisser. Detailed balance limit of efficiency of p-n junction solar cells. *J. Appl. Phys.*, 32:510–519, 1961.
- [5] A. Rao, M. W. B. Wilson, J. Hodgkiss, S. Albert-Seifried, H. Bassler, and H. R. Friend. Exciton fission and charge generation via triplet excitons in pentacene/c-60 bilayers. *J. Am. Chem. Soc.*, 132:12698–12703, 2010.
- [6] M. W. B. Wilson, A. Rao, J. Clark, R. S. S. Kumar, D. Brida, G. Cerullo, and R. H. Friend. Ultrafast dynamics of exciton fission in polycrystalline pentacene. *J. Am. Chem. Soc.*, 133(31):11830–11833, 2011.
- [7] G. Granucci, M. Persico, and A. Toniolo. Direct semiclassical simulation of photochemical processes with semiempirical wave functions. *J. Chem. Phys.*, 114(24):10608–10615, 2001.
- [8] A. Toniolo, C. Ciminelli, G. Granucci, T. Laino, and M. Persico. QM/MM connection atoms for the multistate treatment of organic and biological molecules. *Theor. Chem. Acc.*, 111:270–279, 2004.
- [9] S. Singh, W. J. Jones, W. Siebrand, B. P. Stoicheff, and W. G. Schneider. Laser generation of excitons and fluorescence in anthracene crystals. *J. Chem. Phys.*, 42(1):330–342, 1965.
- [10] C.E. Swenberg and W.T. Stacy. Bimolecular radiationless transitions in crystalline tetracene. *Chem. Phys. Lett.*, 2(5):327–328, 1968.
- [11] I. Paci, J. C. Johnson, X. Chen, G. Rana, D. Popovic, D. E. David, A. J. Nozik, M. A. Ratner, and J. Michl. Singlet fission for dye-sensitized solar cells: Can a suitable sensitizer be found? *J. Am. Chem. Soc.*, 128(51):16546–16553, 2006.
- [12] A. Akdag, Z. Havlas, and J. Michl. Search for a small chromophore with efficient singlet fission: Biradicaloid heterocycles. *J. Am. Chem. Soc.*, 134(35):14624–14631, 2012.
- [13] T. Zeng, N. Ananth, and R. Hoffmann. Seeking small molecules for singlet fission: A heteroatom substitution strategy. *J. Am. Chem. Soc.*, 136(36):12638–12647, 2014.
- [14] J. Wen, Z. Havlas, and J. Michl. Captodatively stabilized biradicaloids as chromophores for singlet fission. *J. Am. Chem. Soc.*, 137(1):165–172, 2015.
- [15] K. Andersson, P. Å. Malmqvist, and B. O. Roos. Second-order perturbation theory with a complete active space self-consistent field reference function. *J. Chem. Phys.*, 96:1218–1226, 1992.
- [16] Andersson K. and B. O. Roos. in D. R., Yarkony, Modern Electronic Structure Theory, Part I, Chapter 2. World Scientific, 1995.

- [17] C. Angeli, R. Cimiraglia, S. Evangelisti, Leininger T., and J. P. Malrieu. Introduction of n-electron valence states for multireference perturbation theory. *J. Chem. Phys.*, 114(23):10252–10264, 2001.
- [18] C. Angeli, R. Cimiraglia, and J. P. Malrieu. n-electron valence state perturbation theory: A spinless formulation and an efficient implementation of the strongly contracted and of the partially contracted variants. *J. Chem. Phys.*, 117(20):9138–9153, 2002.
- [19] C. Angeli, M Pastore, and R. Cimiraglia. New perspectives in multireference perturbation theory: the n-electron valence state approach. *Theor. Chem. Acc.*, 117: 743–754, 2007.
- [20] P.-O. Widmark, P. Å. Malmqvist, and B. O. Roos. Density matrix averaged atomic natural orbital (ANO) basis sets for correlated molecular wave functions - First row atoms. *Theor. Chim. Acta*, 77:291–306, 1990.
- [21] P.-O. Widmark, B. J. Persson, and B. O. Roos. Density matrix averaged atomic natural orbital (ANO) basis sets for correlated molecular wave function - Second row atoms. *Theor. Chim. Acta*, 79:419–432, 1991.
- [22] G. Ghigo, B. O. Roos, and P. Å. Malmqvist. A modified definition of the zeroth-order hamiltonian in multiconfigurational perturbation theory (CASPT2). *Chem. Phys. Letters*, 396:142–149, 2004.
- [23] Molcas 8: New capabilities for multiconfigurational quantum chemical calculations across the periodic table. *J. Comp. Chem.*, 37:506–541, 2016.
- [24] H.-J. Werner, P. J. Knowles, G. Knizia, F. R. Manby, Schutz M., et al. MOLPRO, version 2015.1, a package of ab initio programs.
- [25] D. Rabinovich. Topochemistry. Part xiv. The crystal structure of 2,3-dimethyl-1,4-benzoquinone. *J. Chem. Soc. (B)*, pages 140–144, 1967.
- [26] R. Dovesi, R. Orlando, A. Erba, et al. CRYSTAL14: a program for the ab initio investigation of crystalline solids. *Int. J. Quantum Chem.*, 114(19):1287–1317, 2014.
- [27] S. Grimme. Semiempirical GGA-type density functional constructed with a long-range dispersion correction. *J. Comput. Chem.*, 27(15):1787–1799, 2006.
- [28] H. J. Monkhorst and J. D. Pack. Special points for Brillouin-zone integration. *Phys. Rev. B*, 13:5188, 1976.
- [29] G. Granucci and A. Toniolo. Molecular gradients for semiempirical CI wavefunctions with floating occupation molecular orbitals. *Chem. Phys. Lett.*, 325:79–85, 2000.
- [30] J. J. P. Stewart. Optimization of parameters for semiempirical methods. *J. Comp. Chem.*, 10(2):209–264, 1989.

- [31] The parameters supplied with TINKER are from “OPLS All-Atom parameters for organic molecules, ions, peptides and nucleic acids, July 2008” as provided by W. L. Jorgensen, Yale University during June 2009. These parameters are taken from those distributed with BOSS Version 4.8.
- [32] TINKER — Software tools for molecular design, Version 6.3 February 2014, Copyright (c) Jay William Ponder 1990-2014.
- [33] C. M. Breneman and K. B. Wiberg. Determining atom-centered monopoles from molecular electrostatic potentials. The need for high sampling density in formamide conformational analysis. *J. Comp. Chem.*, 11(3):361–373, 1990.
- [34] R. McWeeny. Methods of molecular quantum mechanics. *Academic Press*, pages 485–491, 1992.
- [35] G. Granucci, M. Persico, and Zocante A. Including quantum decoherence in surface hopping. *J. Chem. Phys.*, 133:134111/1–134111/9, 2010.
- [36] J. J. P. Stewart. MOPAC2000; Fujitsu Limited: Tokyo, Japan. 1999.
- [37] G. Bussi and Parrinello M. Stochastic thermostats: comparison of local and global schemes. *Comp. Phys. Commun.*, 179:26–29, 2008.
- [38] L. Creatini, T. Cusati, G. Granucci, and M. Persico. Photodynamics of azobenzene in a hindering environment. *Chem. Phys.*, 347:492–502, 2008.
- [39] M. Persico and G. Granucci. An overview of nonadiabatic dynamics simulations methods, with focus on the direct approach versus the fitting of potential energy surfaces. *Theor. Chem. Acc.*, 133:1526/1–1526/28, 2014.

# Testing new chromophores for singlet fission: a computational protocol applied to 2,3-diamino-1,4-benzoquinone.

Davide Accomasso<sup>a</sup>, Giovanni Granucci<sup>a</sup>, Remco W. A. Havenith<sup>b,c</sup>,  
Maurizio Persico<sup>a</sup>

<sup>a</sup> Università di Pisa, Dipartimento di Chimica e Chimica Industriale,  
via Moruzzi 13, 56124 Pisa, Italy

<sup>b</sup> Theoretical Chemistry, Zernike Institute for Advanced Materials  
and Stratingh Institute for Chemistry, University of Groningen,  
Nijenborgh 4, 9747 AG Groningen, The Netherlands

<sup>c</sup> Ghent Quantum Chemistry Group, Department of Inorganic and Physical Chemistry,  
Ghent University, Krijgslaan 281 (S3) B-9000 Gent, Belgium

## Supporting Information

### Section S1. Benchmark calculations

To test the CASPT2/ANO-L-VTZP method, the vertical and adiabatic excitation energies for the low-lying electronic states of 1,4-benzoquinone and 2,3-dichloro-1,4-benzoquinone, which are chemically related to the proposed singlet fission chromophore DAP-BQ, were computed and compared with the available experimental values (Tables S1 and S4).

#### Section S1.1. 1,4-benzoquinone

Since the experimental molecular structure of gaseous 1,4-benzoquinone has been characterized [1], it was used as input geometry for the CASPT2/ANO-L-VTZP optimization of  $S_0$ . The excited state optimizations were then performed starting from the ground state equilibrium geometry obtained. All calculations on 1,4-benzoquinone were carried out using the  $D_{2h}$  symmetry. The natural orbitals for the  $S_0$  state at the CASPT2/ANO-L-VTZP optimized ground state geometry are shown in Figure S1. The first two singlet and triplet excited states are mainly  $n \rightarrow \pi^*$  excitations that can be described as electron promotions from the 4  $b_{1g}$  to the 2  $b_{3g}$  orbital ( $1^1B_{2g}$  and  $1^3B_{2g}$ ) and from the 5  $b_{3u}$  to the 2  $b_{3g}$  MO ( $1^1A_u$  and  $1^3A_u$ ). The  $S_3$ ,  $S_4$ ,  $T_3$  and  $T_4$  states are mainly  $\pi \rightarrow \pi^*$  excitations: 1  $b_{2g} \rightarrow 2 b_{3g}$  ( $1^1B_{1g}$  and  $1^3B_{1g}$ ) and 2  $b_{1u} \rightarrow 2 b_{3g}$  ( $1^1B_{2u}$  and  $1^3B_{2u}$ ). Moreover, while in the singlet manifold the  $1^1B_{1g}$  state is lower in energy than the  $1^1B_{2u}$ , in the triplet manifold the order is inverted, the  $1^3B_{2u}$  state being lower than the  $1^3B_{1g}$ . Another relevant finding is the change in the order of the two  $n \rightarrow \pi^*$  states, in the singlet as well as in the triplet manifold, between the vertical and adiabatic excitation; this implies the presence of a conical intersection. This change in the order of the two  $n \rightarrow \pi^*$  states is in line with the calculations performed by Weber et al. [2] and Ter Horst and Kommandeur's experimental findings [7], while it is in contrast with the spectroscopic data provided by Trommsdorff et al. [4, 5].

Considering only the experimental value which refers to the vapor phase spectrum when more than one spectroscopic data is available (Table S1, experimental values in bold), the

computed excitation energies exhibit a mean absolute deviation from the experimental values less than 0.1 eV (0.098 eV). The maximum absolute deviation is 0.32 eV, associated with the vertical excitation energy of the  $1^1B_{1g}$  state, which is underestimated by the CASPT2/ANO-L-VTZP method.

Table S1: CASSCF and CASPT2/ANO-L-VTZP vertical and adiabatic excitation energies (in eV) evaluated at CASPT2/ANO-L-VTZP optimized geometries for 1,4-benzoquinone. The  $D_{2h}$  symmetry was used. The experimental values in bold were selected to evaluate the difference with the computed results (see the text).

State label	Nature	Vertical		Exp. value	Adiabatic		Exp. value
		CASSCF	CASPT2		CASSCF	CASPT2	
$1^1B_{2g}$	$n \rightarrow \pi^*$	4.21	2.69	<b>2.70<sup>a</sup></b>	3.87	2.47	<b>2.49<sup>b, c, d</sup></b>
$1^1A_u$	$n \rightarrow \pi^*$	4.18	2.71	<b>2.70<sup>a</sup></b>	3.79	2.36	2.52 <sup>b</sup> 2.49 <sup>c</sup> <b>2.48<sup>d</sup></b>
$1^1B_{1g}$	$\pi \rightarrow \pi^*$	5.89	4.28	4.41 <sup>e</sup> 4.40 <sup>f</sup> 4.42 <sup>g</sup> <b>4.6<sup>h</sup></b> 4.48 <sup>i</sup>	5.42	3.79	<b>4.07<sup>l</sup></b>
$1^1B_{2u}$	$\pi \rightarrow \pi^*$	7.46	5.34	5.41 <sup>e</sup> <b>5.4<sup>h, m</sup></b>	7.26	5.15	<b>5.12<sup>l</sup></b>
$1^3B_{2g}$	$n \rightarrow \pi^*$	3.97	2.49	-	3.72	2.32	2.31 <sup>b</sup> <b>2.28<sup>n</sup></b> 2.313 <sup>o</sup> 2.307 <sup>p</sup>
$1^3A_u$	$n \rightarrow \pi^*$	3.97	2.53	-	3.64	2.22	2.35 <sup>b</sup> <b>2.32<sup>n, q, r, s, t</sup></b> 2.314 <sup>o</sup> 2.35 <sup>p</sup>
$1^3B_{2u}$	$\pi \rightarrow \pi^*$	3.48	3.07	$\approx$ <b>3.0<sup>u</sup></b>	3.20	2.55	$\approx$ <b>2.67<sup>b</sup></b>
$1^3B_{1g}$	$\pi \rightarrow \pi^*$	3.69	3.41	-	3.35	3.01	-

<sup>a</sup> Absorption spectrum in cyclohexane, maximum of the unresolved band for both  $1^1B_{2g}$  and  $1^1A_u$  transitions [3].

<sup>b</sup> Single crystal absorption spectrum at 4.2 K, 0-0 transition [4, 5].

<sup>c</sup> Crystal absorption spectrum at 1.8 K, 0-0 transition [6].

<sup>d</sup> Supersonic jet fluorescence excitation spectrum, 0-0 transition [7].

<sup>e</sup> Vapor phase absorption spectrum at room temperature, absorption maximum [8].

<sup>f</sup> Absorption spectrum in cyclohexane, band maximum [3].

<sup>g</sup> MCD (magnetic circular dichroism) spectrum in n-hexane [9].

<sup>h</sup> Gas phase absorption, band maximum [10].

<sup>i</sup> Absorption spectrum in n-hexane or hexafluoroisopropanol [11].

<sup>l</sup> Vapor phase absorption spectrum at room temperature, 0-0 transition [5, 8].

<sup>m</sup> EEL (electron energy loss) vapor phase spectrum, band maximum, 20 eV residual energy [12].

<sup>n</sup> Vapor phase phosphorescence spectra at 90°C in the presence of argon, 0-0 transition [13].

<sup>o</sup> Phosphorescence in Ne-matrix [14].

<sup>p</sup> Phosphorescence and ODMR spectra of pure h<sub>4</sub>-PBQ crystals, oscillator strength for  $1^3B_{2g}$  state is  $3.0 \cdot 10^{-9}$ .

<sup>q</sup> Vapor phase absorption spectrum, 0-0 transition [5].

<sup>r</sup> Vapor phase absorption spectrum at  $\approx 100^\circ\text{C}$  [16].

<sup>s</sup> Vapor phase emission spectra at 25°C [17].

<sup>t</sup> Phosphorescence excitation spectrum in jet [18].

<sup>u</sup> Gas phase EEL (electron energy loss) spectrum [12].

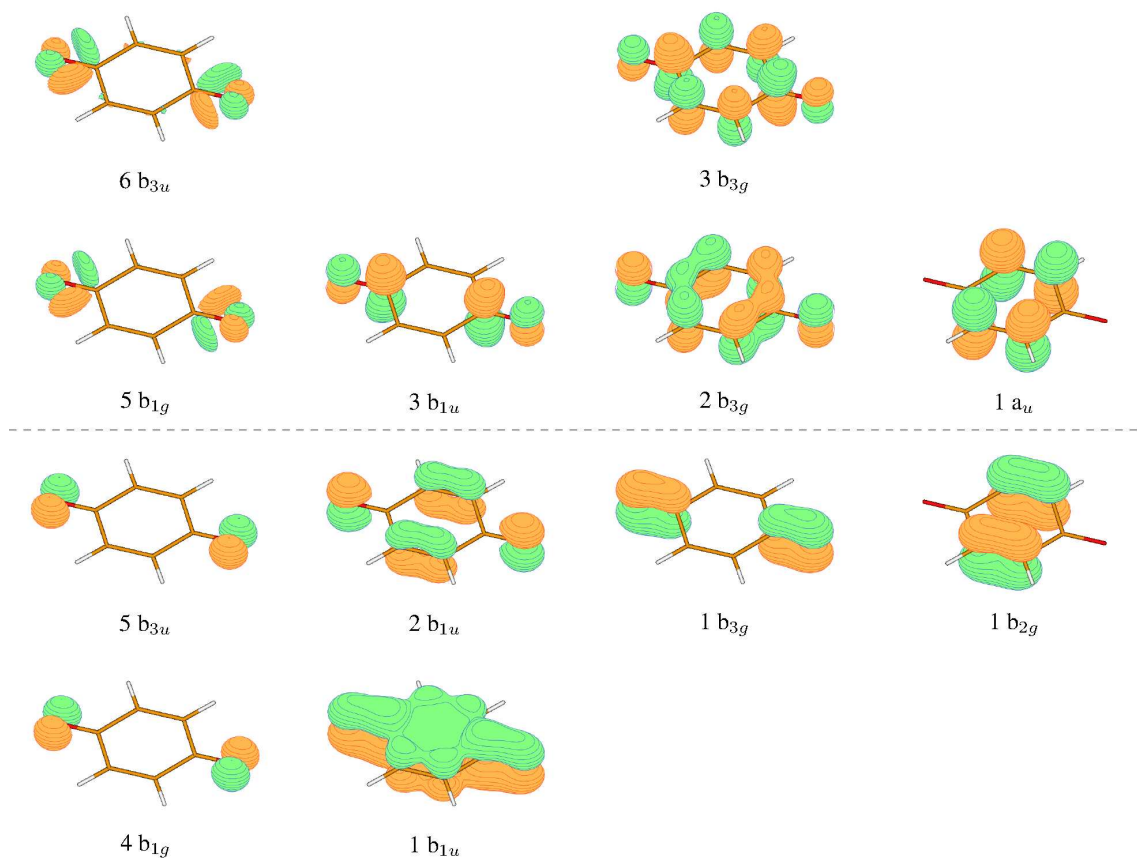


Figure S1: Natural orbitals for  $S_0$  at the CASPT2/ANO-L-VTZP optimized ground state geometry of 1,4-benzoquinone. The dashed line separates the orbitals with occupation numbers close to 0 (above) and close to 2 (below).

In Tables S2 and S3 the CASPT2/ANO-L-VTZP optimized geometries for the first 5 singlets and 4 triplets are shown, together with the experimental ground state molecular structure [1]. The calculated equilibrium geometry of  $S_0$  is in good agreement with the experimental data. In the excited states the C=O and C=C bonds are longer than in the ground state, as would be expected from transitions where an electron is promoted from a non-bonding orbital (for the  $1^1B_{2g}$ ,  $1^1A_u$ ,  $1^3B_{2g}$ ,  $1^3A_u$  states) or a mainly C=C bonding orbital (for the  $1^1B_{1g}$ ,  $1^1B_{2u}$ ,  $1^3B_{2u}$  and  $1^3B_{1g}$  states) to the  $2 b_{3g}$  orbital (Figure S1), which is mainly C=C and C=O antibonding. Moreover, the two C-C distances decrease; in fact, the  $2 b_{3g}$  orbital is C-C bonding.

Table S2: CASPT2/ANO-L-VTZP optimized geometries for the first five electronic singlet states of 1,4-benzoquinone. Bond distances ( $r$ ) in Angstroms, angles ( $\angle$ ) in degrees.

Parameter	Exp. <sup>a</sup>	CASPT2/ANO-L-VTZP				
	1 <sup>1</sup> A <sub>g</sub>	1 <sup>1</sup> A <sub>g</sub>	1 <sup>1</sup> B <sub>2g</sub>	1 <sup>1</sup> A <sub>u</sub>	1 <sup>1</sup> B <sub>1g</sub>	1 <sup>1</sup> B <sub>2u</sub>
$r(\text{C}=\text{O})$	1.225 (0.002)	1.225	1.280	1.283	1.261	1.256
$r(\text{C}=\text{C})$	1.344 (0.003)	1.347	1.370	1.379	1.418	1.391
$r(\text{C}-\text{C})$	1.481 (0.002)	1.478	1.433	1.426	1.436	1.458
$r(\text{C}-\text{H})$	1.089 (0.011)	1.081	1.080	1.081	1.084	1.082
$\angle(\text{C}-\text{C}-\text{C})$	118.1 (0.3)	117.8	118.4	119.6	113.9	117.8
$\angle(\text{C}=\text{C}-\text{H})$	121.4 (assumed) <sup>b</sup>	122.7	121.4	121.4	119.6	122.1

<sup>a</sup> Molecular structure of gaseous 1,4-benzoquinone determined by electron diffraction [1].

<sup>b</sup> Value found in ethylene [19].

Table S3: CASPT2/ANO-L-VTZP optimized geometries for the first four electronic triplet states of 1,4-benzoquinone. Bond distances ( $r$ ) in Angstroms, angles ( $\angle$ ) in degrees.

Parameter	CASPT2/ANO-L-VTZP			
	1 <sup>3</sup> B <sub>2g</sub>	1 <sup>3</sup> A <sub>u</sub>	1 <sup>3</sup> B <sub>2u</sub>	1 <sup>3</sup> B <sub>1g</sub>
$r(\text{C}=\text{O})$	1.270	1.278	1.301	1.240
$r(\text{C}=\text{C})$	1.364	1.376	1.393	1.422
$r(\text{C}-\text{C})$	1.438	1.428	1.422	1.449
$r(\text{C}-\text{H})$	1.080	1.081	1.080	1.082
$\angle(\text{C}-\text{C}-\text{C})$	118.0	119.6	119.8	114.1
$\angle(\text{C}=\text{C}-\text{H})$	121.4	121.4	122.0	120.1

### Section S1.2. 2,3-dichloro-1,4-benzoquinone

Since the experimental gas phase molecular structure of 2,3-dichloro-1,4-benzoquinone is not available in the literature, the input geometry for the optimization of  $S_0$  was obtained from the ground state CASPT2/ANO-L-VTZP optimized geometry of 1,4-benzoquinone replacing the two hydrogens in positions 2 and 3 with two chlorine atoms. The geometry optimizations, for the ground state as well as for the excited states, were performed using the  $C_{2v}$  symmetry. Figure S2 shows the natural orbitals for  $S_0$  at the ground state CASPT2/ANO-L-VTZP optimized geometry. Note that four  $\sigma(\text{CO})$  (orbitals 4  $b_{1g}$ , 5  $b_{3u}$ , 5  $b_{1g}$  and 6  $b_{3u}$  in Figure S1) replace the four oxygen lone pairs found in the active space of 1,4-benzoquinone. The excited states 1<sup>1</sup>B<sub>2</sub> and 1<sup>3</sup>B<sub>2</sub>, mainly of  $\pi \rightarrow \pi^*$  character, share the same active orbitals of  $S_0$ . At variance, for the 1<sup>1</sup>B<sub>1</sub>, 1<sup>3</sup>B<sub>1</sub>, 1<sup>1</sup>A<sub>2</sub> and 1<sup>3</sup>A<sub>2</sub> states, mainly of  $n \rightarrow \pi^*$  nature, the four  $\sigma(\text{CO})$  in the  $S_0$  active space are replaced with four oxygen lone pairs. As in 1,4-benzoquinone, the first two singlet and triplets excited states of 2,3-dichloro-1,4-benzoquinone are mainly  $n \rightarrow \pi^*$  excitations that can be described as electron promotions from a lone pair orbital in  $b_2$  symmetry (similar to the 4  $b_{1g}$  orbital in Figure S1) to the 4  $a_2$  orbital (1<sup>1</sup>B<sub>1</sub> and 1<sup>3</sup>B<sub>1</sub>) and from a lone pair orbital in  $a_1$  symmetry (similar to the 5  $b_{3u}$  orbital in Figure S1) to the 4  $a_2$  orbital (1<sup>1</sup>A<sub>2</sub> and 1<sup>3</sup>A<sub>2</sub>). These four excited states are slightly higher in energy (about 0.1 eV) in 2,3-dichloro-1,4-benzoquinone compared to 1,4-benzoquinone. Moreover, the order of the two  $n \rightarrow \pi^*$

states, in the singlet as well as in the triplet manifold, changes between the vertical and adiabatic excitation, as already noticed for 1,4-benzoquinone. The  $S_3$  and  $T_3$  states are mainly  $\pi \rightarrow \pi^*$  excitations that are reasonably described as electron promotions from the  $5 b_1$  to the  $4 a_2$  orbital ( $1^1B_2$  and  $1^3B_2$ ). Compared to 1,4-benzoquinone, these excitations are considerably lower in energy.

The mean absolute deviation of the calculated CASPT2 excitation energies from the available experimental values is 0.08 eV with a maximum deviation of 0.21 eV for the adiabatic excitation energy of the  $1^1B_2$  state.

Table S4: CASSCF and CASPT2/ANO-L-VTZP vertical and adiabatic excitation energies (in eV) evaluated at CASPT2/ANO-L-VTZP optimized geometries for 2,3-dichloro-1,4-benzoquinone. The  $C_{2v}$  symmetry was used. The computed energies are compared with spectroscopic data.

State label	Nature	Vertical		Exp. value	Adiabatic		Exp. value
		CASSCF	CASPT2		CASSCF	CASPT2	
$1^1B_1$	$n \rightarrow \pi^*$	4.87	2.80	-	4.51	2.52	2.60 <sup>a</sup>
$1^1A_2$	$n \rightarrow \pi^*$	4.89	2.85	-	4.46	2.48	-
$1^1B_2$	$\pi \rightarrow \pi^*$	5.63	3.71	3.73 <sup>b</sup>	5.19	3.21	3.42 <sup>b</sup>
$1^3B_1$	$n \rightarrow \pi^*$	4.63	2.60	-	4.35	2.37	2.30 <sup>a</sup>
$1^3A_2$	$n \rightarrow \pi^*$	4.67	2.68	-	4.31	2.34	2.30 <sup>a</sup>
$1^3B_2$	$\pi \rightarrow \pi^*$	3.39	2.91	-	2.81	2.40	-

<sup>a</sup> Single crystal absorption spectrum at 4.2 K, 0-0 transition [4, 5].

<sup>b</sup> Vapor phase absorption spectrum at room temperature, 0-0 transition [5, 8].

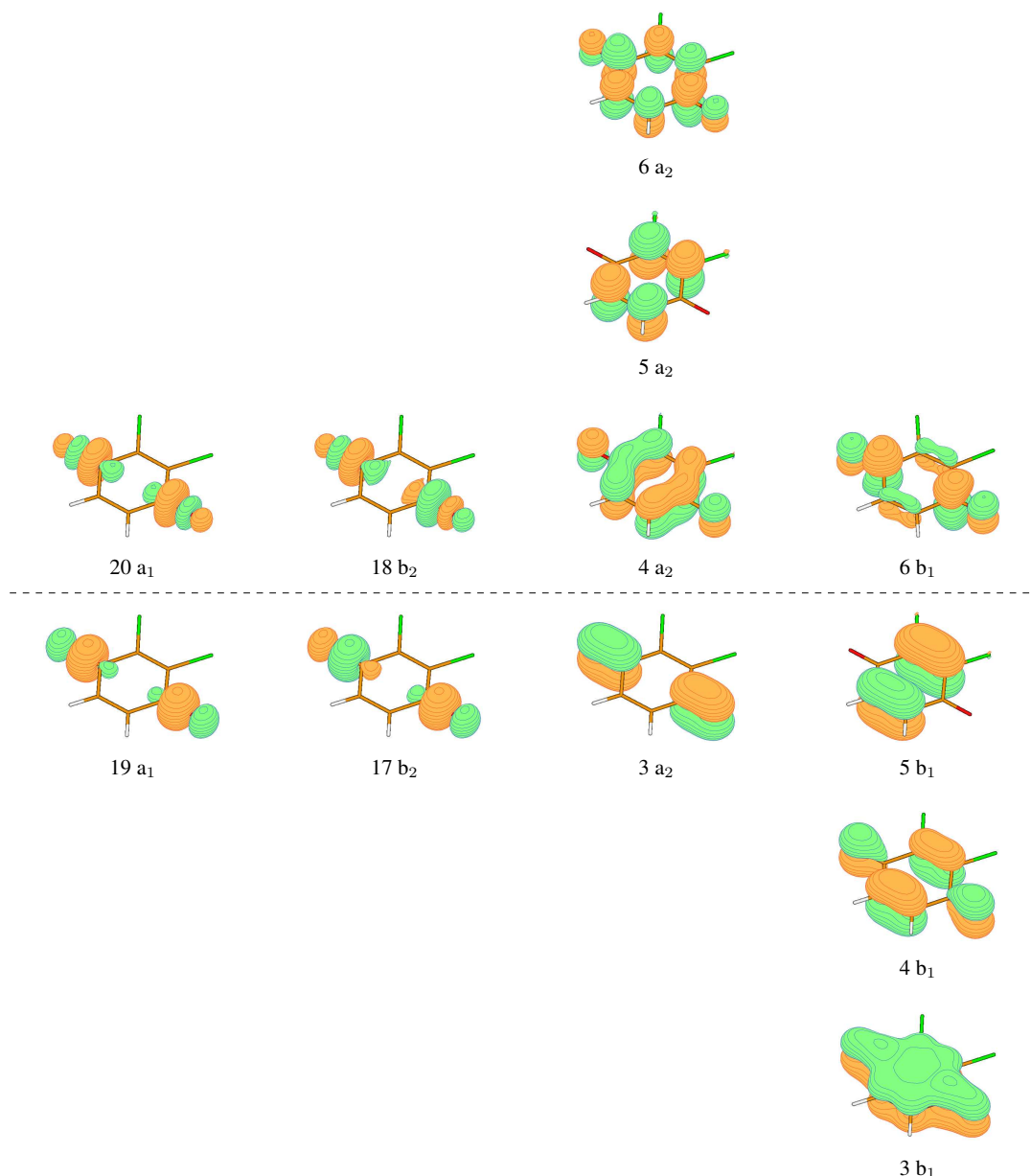


Figure S2: Natural orbitals for  $S_0$  at the CASPT2/ANO-L-VTZP optimized ground state geometry of 2,3-dichloro-1,4-benzoquinone. The dashed line separates the orbitals with occupation numbers close to 0 (above) and close to 2 (below).

### Section S1.3. Discussion

From the benchmark calculations on 1,4-benzoquinone and 2,3-dichloro-1,4-benzoquinone it turned out that the CASPT2/ANO-L-VTZP method reproduces very well the excitation energies of the  $n \rightarrow \pi^*$  states, while it tends to underestimate the energy of the first singlet  $\pi \rightarrow \pi^*$  excitation. In particular, the adiabatic excitation energy of the first singlet  $\pi \rightarrow \pi^*$  transition is underestimated by 0.28 in 1,4-benzoquinone and by 0.21 eV in 2,3-dichloro-1,4-benzoquinone.

Moreover, it is worth noting that the CASPT2 corrections on the CASSCF relative energies are quite large and variable for the  $\pi \rightarrow \pi^*$  states (from about -0.3 to -2.1 eV for 1,4-benzoquinone and from about -0.4 and -2 for 2,3-dichloro-1,4-benzoquinone), while

being nearly constant for the  $n \rightarrow \pi^*$  states (about -1.5 eV for 1,4-benzoquinone and about -2 eV for 2,3-dichloro-1,4-benzoquinone).

## Section S2. Ab initio calculations on DAPBQ molecule

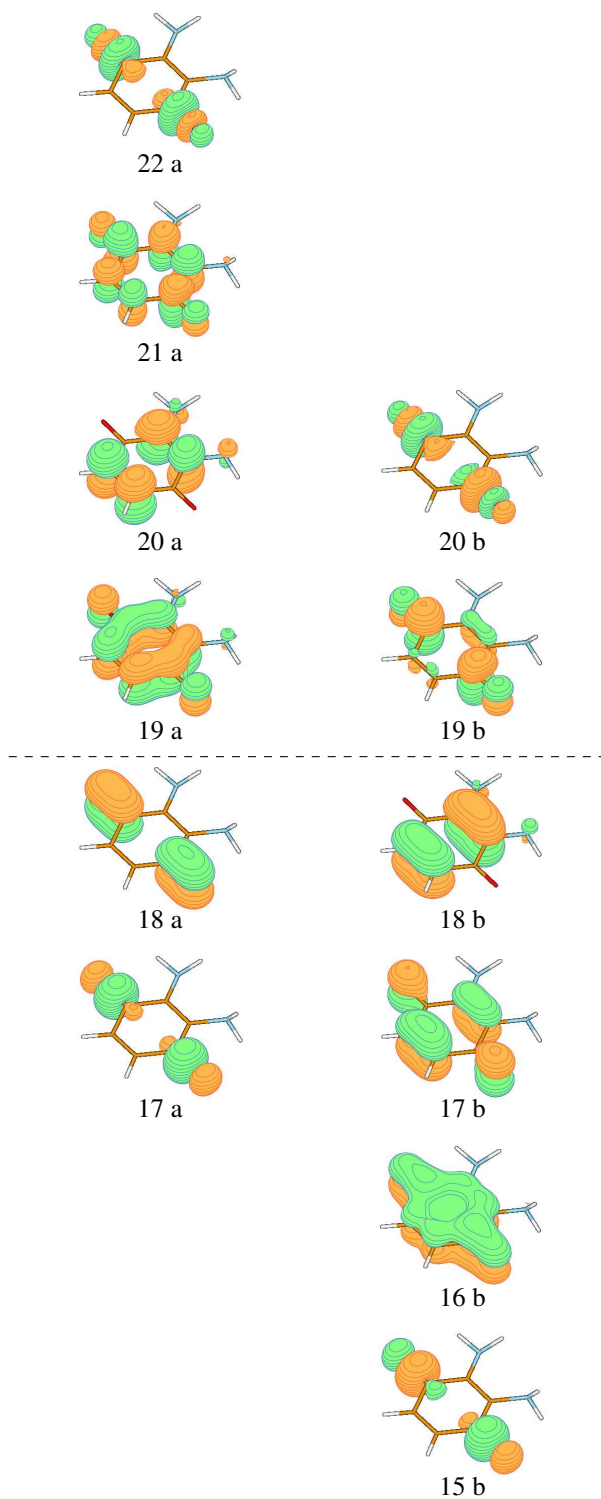


Figure S3: Natural orbitals for  $S_0$  at the CASPT2/ANO-L-VTZP optimized ground state geometry of DAPBQ. The dashed line separates the orbitals with occupation numbers close to 0 (above) and close to 2 (below).

CASPT2/ANO-L-VTZP optimized geometries of DAPBQ (atomic coordinates in Angstroms).  
 The ground state geometry optimization was performed starting from the CASPT2/ANO-S-VDZP optimized geometry for  $S_0$  reported by Wen et al. [14].

$S_0$

C	-0.67772597	-0.26287802	0.06987610
C	0.67772597	-0.26287802	-0.06987610
C	-1.42267380	-1.52477207	0.12911239
C	1.42267380	-1.52477207	-0.12911239
C	-0.66968955	-2.79511680	0.05103579
C	0.66968955	-2.79511680	-0.05103579
H	-1.25773098	-3.70031090	0.09596547
H	1.25773098	-3.70031090	-0.09596547
O	-2.64378952	-1.51981436	0.26117030
O	2.64378952	-1.51981436	-0.26117030
N	-1.41385573	0.90701686	0.10907008
N	1.41385573	0.90701686	-0.10907008
H	-0.98756093	1.65225383	0.64173200
H	0.98756093	1.65225383	-0.64173200
H	-2.37672404	0.74162346	0.36838903
H	2.37672404	0.74162346	-0.36838903

$S_1$

C	-0.69189740	-0.26551291	0.09892708
C	0.69189740	-0.26551291	-0.09892708
C	-1.45177663	-1.54460748	0.20824718
C	1.45177663	-1.54460748	-0.20824718
C	-0.69248870	-2.72581879	0.09917989
C	0.69248870	-2.72581879	-0.09917989
H	-1.22891713	-3.66176094	0.17600745
H	1.22891713	-3.66176094	-0.17600745
O	-2.69309715	-1.43954370	0.38666662
O	2.69309715	-1.43954370	-0.38666662
N	-1.46999223	0.80688480	0.21005505
N	1.46999223	0.80688480	-0.21005505
H	-1.15975961	1.76055801	0.16439072
H	1.15975961	1.76055801	-0.16439072
H	-2.45195954	0.56780303	0.35108842
H	2.45195954	0.56780303	-0.35108842

T<sub>1</sub>

C	-0.70265844	-0.27834393	0.09826983
C	0.70265844	-0.27834393	-0.09826983
C	-1.45284708	-1.53586653	0.20061402
C	1.45284708	-1.53586653	-0.20061402
C	-0.68525564	-2.73241690	0.09427836
C	0.68525564	-2.73241690	-0.09427836
H	-1.22660880	-3.66561142	0.16913353
H	1.22660880	-3.66561142	-0.16913353
O	-2.69433474	-1.45125955	0.37354733
O	2.69433474	-1.45125955	-0.37354733
N	-1.46018491	0.80834566	0.20586291
N	1.46018491	0.80834566	-0.20586291
H	-1.13007369	1.75472180	0.17489331
H	1.13007369	1.75472180	-0.17489331
H	-2.44647377	0.59843287	0.34610655
H	2.44647377	0.59843287	-0.34610655

### Section S3. Computed crystal structure of DAPBQ

Unit cell atomic coordinates (in Angstroms) of the computed (B3LYP-D/6-21G) crystal structure of DAPBQ (cell parameters are reported in the main text, Table 2):

O	2.011758	-1.738385	-0.807930	molecule A
O	4.046294	2.067936	-4.067135	
C	2.491630	-0.828718	-1.540940	
C	1.831537	-0.493281	-2.816709	
C	2.306458	0.518105	-3.618350	
C	3.552780	1.177163	-3.303888	
C	4.239262	0.812107	-2.035679	
C	3.730989	-0.107319	-1.202298	
H	5.168605	1.342065	-1.859236	
H	4.183492	-0.375833	-0.255149	
N	0.741199	-1.228370	-3.193939	
N	1.594636	0.860488	-4.773337	
H	0.367759	-1.957546	-2.571345	
H	0.628043	-1.373817	-4.203936	
H	2.022457	1.573836	-5.385420	
H	0.598667	1.040220	-4.579553	
O	-3.807677	-2.075079	-0.825969	molecule B
O	-0.689588	1.741194	-3.049555	
C	-3.079902	-1.178265	-1.357213	
C	-3.470564	-0.518248	-2.584863	
C	-2.701630	0.494060	-3.108193	
C	-1.394044	0.832487	-2.524618	
C	-0.980382	0.116976	-1.302687	

C	-1.776264	-0.807642	-0.746361	
H	-0.011541	0.395729	-0.904687	
H	-1.546413	-1.334970	0.172794	
N	-4.659936	-0.869519	-3.223770	
N	-3.149506	1.224460	-4.179180	
H	-5.245899	-1.586094	-2.765431	
H	-4.536119	-1.027420	-4.233962	
H	-2.550338	1.953521	-4.587126	
H	-4.163474	1.386454	-4.212626	
O	-1.050265	2.067979	1.326163	molecule C
O	-3.091300	-1.736989	4.584122	
C	-2.609091	-0.828691	3.850631	
C	-3.267554	-0.492577	2.574909	
C	-2.790695	0.518787	1.774098	
C	-1.543809	1.177185	2.089341	
C	-0.858217	0.810194	3.357411	
C	-1.368378	-0.109022	4.189945	
H	0.072247	1.338003	3.534845	
H	-0.915648	-0.378820	5.136619	
N	-4.359050	-1.225508	2.194624	
N	-3.500863	0.862811	0.619462	
H	-4.738028	-1.953128	2.816030	
H	-4.466840	-1.372686	1.184224	
H	-3.073815	1.576750	0.007521	
H	-4.497632	1.039478	0.811430	
O	4.405812	1.742213	1.768542	molecule D
O	1.285521	-2.074952	3.987950	
C	2.014972	-1.179039	3.458030	
C	1.625310	-0.518296	2.229831	
C	2.394824	0.493461	1.706500	
C	3.701435	0.832039	2.291231	
C	4.114867	0.114879	3.512442	
C	3.318987	-0.809926	4.068430	
H	5.083937	0.392418	3.910472	
H	3.549787	-1.337953	4.986850	
N	0.435653	-0.869118	1.592274	
N	1.946386	1.223723	0.634840	
H	-0.149337	-1.586940	2.049791	
H	0.555128	-1.020494	0.580847	
H	2.546144	1.952235	0.226647	
H	0.932825	1.389014	0.604411	

Molecule A, B C and D refer to Figure S6.

## Section S4. Parameters choice

Table S6: Vertical and adiabatic excitation energies (in eV) of DAPBQ.

State	Vertical		Adiabatic	
	PM3, (6,4)	CASPT2 [14]	PM3, (6,4)	CASPT2 [14]
S <sub>1</sub>	2.87	2.63	2.27	2.23
T <sub>1</sub>	1.91	1.89	1.17	1.12

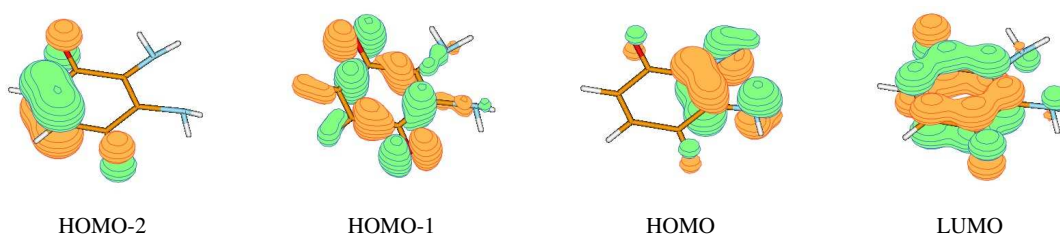


Figure S4: Molecular orbitals of the active space (6,4) at the PM3 optimized ground state geometry. Iso-surface at 0.14 au.

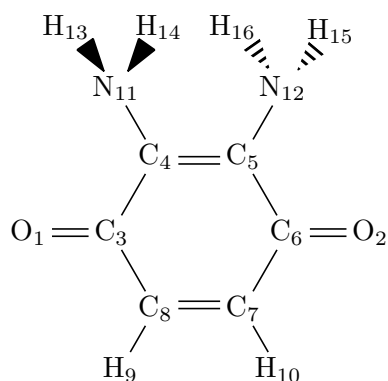


Figure S5: Molecular structure, with atom labels, of DAPBQ.

Table S7: Atom types selected for the MM molecules. Force field: OPLS-AA, as implemented in the TINKER 6.3 [32] molecular modeling package. Atom labels (first column) refer to the molecular structure of Figure S5.

Atom	Atom type	Atom class	Description
O <sub>1</sub> , O <sub>2</sub>	223	4	Ketone C=O
C <sub>4</sub> , C <sub>5</sub>	86	47	Alkene R2-C=
C <sub>3</sub> , C <sub>6</sub>	173	3	Benzophenone C=O
C <sub>7</sub> , C <sub>8</sub>	87	47	Alkene RH-C=
H <sub>9</sub> , H <sub>10</sub>	89	46	Alkene H-C=
N <sub>11</sub> , N <sub>12</sub>	730	44	Amine RNH2
H <sub>13</sub> , H <sub>14</sub> , H <sub>15</sub> , H <sub>16</sub>	739	45	Amine RNH2

Table S8: Atomic charges for the MM molecules determined at the CAM-B3LYP/TZVP level using the CHELPG scheme with the additional constraint of reproducing the overall molecular dipole moment. Atomic labels refer to Figure S5.

Atom	Atomic charge (a.u.)
O <sub>1</sub> , O <sub>2</sub>	-0.509446
C <sub>4</sub> , C <sub>5</sub>	0.033641
C <sub>3</sub> , C <sub>6</sub>	0.597242
C <sub>7</sub> , C <sub>8</sub>	-0.246323
H <sub>9</sub> , H <sub>10</sub>	0.159674
N <sub>11</sub> , N <sub>12</sub>	-0.720351
H <sub>13</sub> , H <sub>14</sub> , H <sub>15</sub> , H <sub>16</sub>	0.3427815

Table S9: Comparison between the geometry optimized with the OPLS-AA force field and the CASPT2/ANO-L-VTZP optimized geometry for the ground state. Point group C<sub>2</sub>. Bond distances ( $r$ ) in Angstroms, angles ( $\angle$ ) and dihedrals ( $d$ ) in degrees. Atom labels refer to Figure S5.

Internal coordinate	OPLS-AA	CASPT2/ANO-L-VTZP
$r(\text{C}_4-\text{C}_5)$	1.359	1.363
$r(\text{C}_8-\text{C}_7)$	1.354	1.343
$r(\text{C}_3-\text{C}_4)$	1.467	1.467
$r(\text{C}_3-\text{C}_8)$	1.455	1.479
$r(\text{C}_3-\text{O}_1)$	1.229	1.228
$r(\text{C}_4-\text{N}_{11})$	1.349	1.383
$r(\text{N}_{11}-\text{H}_{13})$	1.014	1.011
$r(\text{N}_{11}-\text{H}_{14})$	1.009	1.010
$r(\text{C}_8-\text{H}_9)$	1.079	1.080
$\angle(\text{C}_4-\text{C}_3-\text{C}_8)$	116.8	118.6
$\angle(\text{C}_3-\text{C}_8-\text{C}_7)$	121.8	120.8
$\angle(\text{C}_3-\text{C}_4-\text{C}_5)$	121.4	120.6
$\angle(\text{O}_1-\text{C}_3-\text{C}_4)$	121.5	120.4
$\angle(\text{O}_1-\text{C}_3-\text{C}_8)$	121.8	121.0
$\angle(\text{N}_{11}-\text{C}_4-\text{C}_5)$	120.2	122.2
$d(\text{O}_1-\text{C}_3-\text{C}_4-\text{N}_{11})$	-0.6	-2.8
$d(\text{C}_5-\text{C}_4-\text{C}_3-\text{C}_8)$	-0.5	0.8
$d(\text{C}_4-\text{C}_3-\text{C}_8-\text{C}_7)$	0.1	1.0
$d(\text{H}_{13}-\text{N}_{11}-\text{C}_4-\text{C}_3)$	11.5	12.0
$d(\text{H}_{14}-\text{N}_{11}-\text{C}_4-\text{C}_3)$	137.4	142.1

### Section S5. Identification of the different pairs of neighbouring molecules in the crystal structure

In the crystal structure computed at the DFT level (see Section 2) 15 different pairs of neighbouring molecules were identified. Since the space group of the crystal structure is P<sub>1</sub>, the four molecules in unit cell are not identical by symmetry. They can be labeled as shown in Figure S6. While molecules B and D are approximately on the same plane, molecules A and C are on different, approximately parallel, planes. The distance between two consecutive planes is about 3 Å. Inside the unit cell five different dimers can

be identified, i.e. BA, CD, DA, DB, CB (Figure S6). If the molecules of the unit cells translated along the three crystalline axes are considered as well, ten more different pairs of neighbours can be found, i.e.  $AB_a$ ,  $DC_a$  and  $AC_a$  along the a axis (Figure S7),  $DA_c$ ,  $CB_c$  and  $CA_c$  along c (Figure S8),  $AA_b$ ,  $BB_b$ ,  $CC_b$  and  $DD_b$  along b (Figure S9).

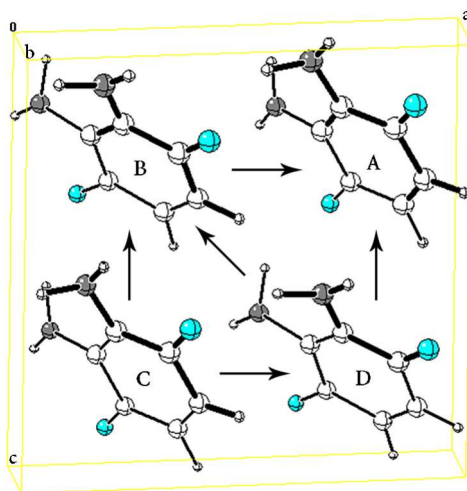


Figure S6: Unit cell of the crystal structure. The different dimers are indicated by arrows.

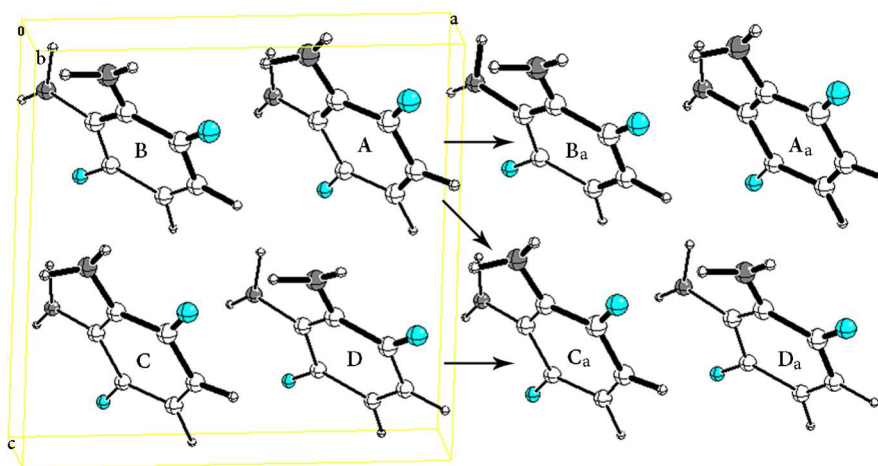


Figure S7: Structure obtained by replicating the unit cell along the a crystalline axis. Each arrow indicates a different dimer.

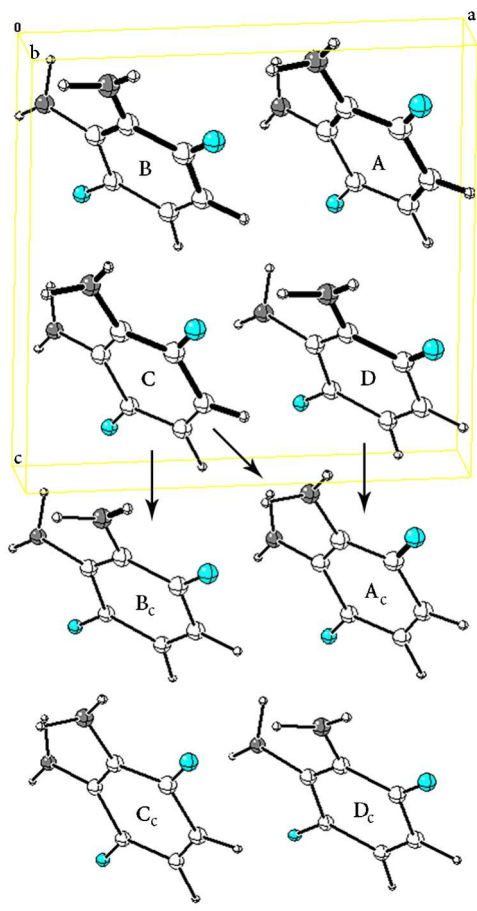


Figure S8: Structure obtained by replicating the unit cell along the c crystalline axis. Each arrow indicates a different dimer.

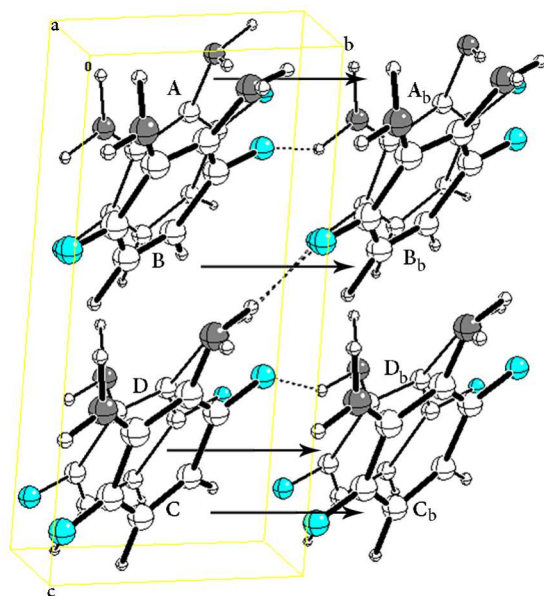


Figure S9: Structure obtained by replicating the unit cell along the b crystalline axis. Each arrow indicates a different dimer.

## Section S6. Selection of the QM dimer

Table S10: Absolute value of  $\langle S_0 S_0 | \hat{\mu} |^1(T_1 T_1) \rangle$  (in debye) for each of the different dimers identified in the crystal structure.

Dimer	$ \langle S_0 S_0   \hat{\mu}  ^1(T_1 T_1) \rangle $
BA	0.010
CD	0.071
DA	0.134
DB	0.003
CB	0.234
AB <sub>a</sub>	0.207
DC <sub>a</sub>	0.273
AC <sub>a</sub>	0.003
DA <sub>c</sub>	0.109
CB <sub>c</sub>	0.099
CA <sub>c</sub>	0.014
AA <sub>b</sub>	0.004
BB <sub>b</sub>	0.003
CC <sub>b</sub>	0.004
DD <sub>b</sub>	0.003

## Section S7. QM/MM simulation of excited state dynamics

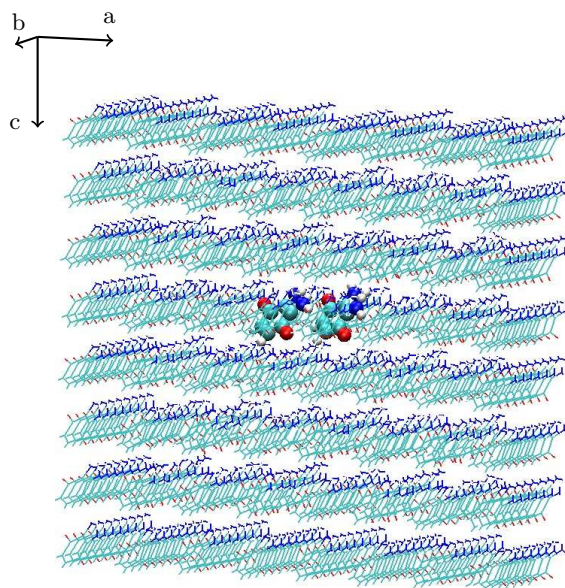


Figure S10: A different view of the approximately cubic cluster for the QM/MM simulation. The QM dimer is represented with ball atoms and stick bonds, while the MM molecules are shown in simple line drawing.

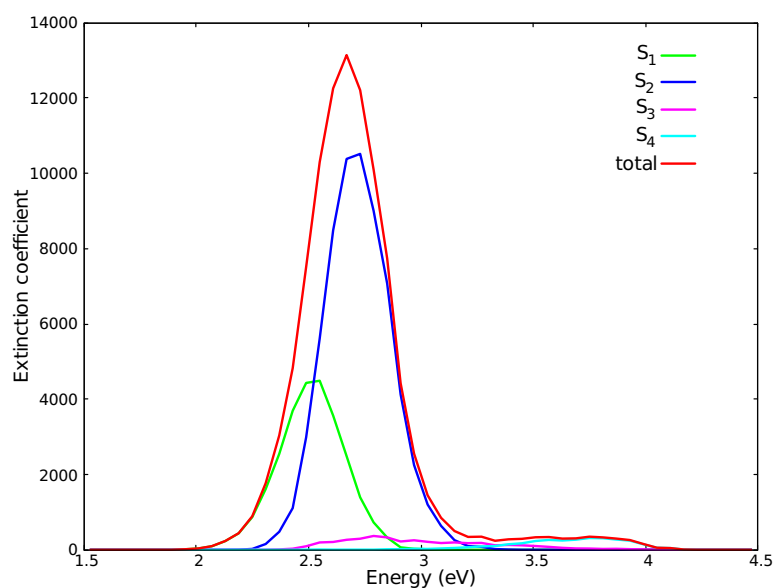


Figure S11: Spectrum of the QM dimer from the QM/MM thermal equilibration on  $S_0$ .

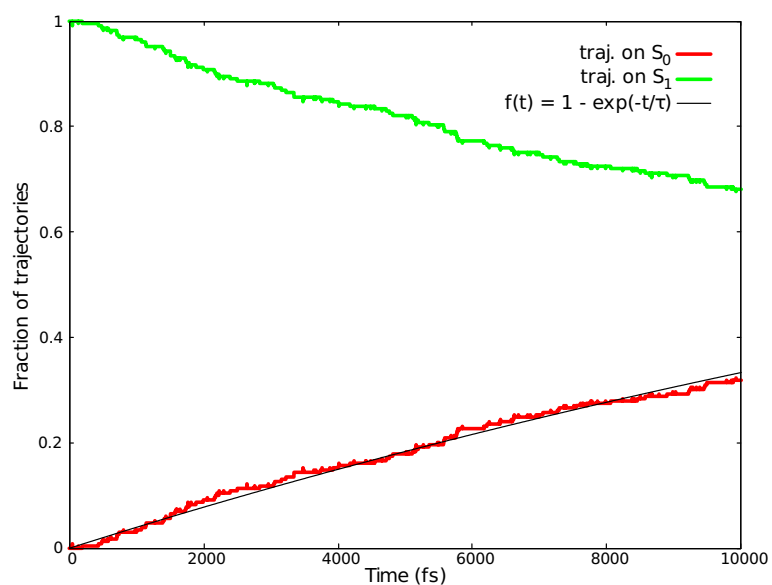


Figure S12: Fraction of trajectories on the  $S_0$  and  $S_1$  states in the QM simulation for one molecule as function of time. The red curve is fitted by an exponential function  $1 - e^{-t/\tau}$ , with  $\tau \simeq 25$  ps.

- [1] Hagen, K.; Hedberg, K. *J. Chem. Phys.* 1973, 59, 158.
- [2] Weber, J.; Malsch K.; Hohlneicher G. *Chem. Phys.* 2001, 264, 275.
- [3] Brand, J. C. D.; Goodwin, T. H. *Trans. Faraday Soc.* 1957, 53, 295.
- [4] Trommsdorff, H. P.; Sahy, P.; Kahane-Pailous, J. *Spectrochimica Acta* 1970, 26A, 1135.

- [5] Trommsdorff, H. P. *J. Chem. Phys.* 1972, 56, 5358.
- [6] Dunn, T. M.; Francis, A. H. *J. Mol. Spect.* 1974, 50, 14.
- [7] Ter Horst, G.; Kommandeur, J. *Chem. Phys.* 1979, 44, 287.
- [8] Trommsdorff, H. P.; Kahane-Paillous, J. *Spectrochimica Acta* 1967, 23A, 1661.
- [9] Meier, A. R.; Wangnière, G. H.; *Chem. Phys.* 1987, 113, 287.
- [10] Brint, P.; Connerade, J.-P.; Tsekeris, T.; Bolovinos, A.; Baig, A. *J. Chem. Soc., Faraday Trans. 2* 1986, 82, 367.
- [11] Kuboyama, A.; Matsuzaki, S.; Tagaki, H.; Arano, H. *Bull. Chem. Soc. Jpn.* 1974, 47, 1601.
- [12] Allan, M. *Chem. Phys.* 1984, 84, 311.
- [13] Koyanagi, M.; Kogo, Y.; Kanda, Y. *Mol. Phys.* 1971, 20, 747.
- [14] Goodman, J.; Brus, L. *J. Chem. Phys.* 1978, 69, 1604.
- [15] Veenvliet, H.; Wiersma, D. A. *Chem. Phys.* 1975, 8, 432.
- [16] Hollas, J. M. *Spectrochim. Acta* 1964, 20, 1563.
- [17] Jayswal, M. G.; Singh, R. S. *Spectrochim. Acta* 1965, 21, 1597.
- [18] Suzuka, I.; Sanekata, M.; Ito, M.; Ohta, N. *Laser Chem.* 1994, 14, 143.
- [19] Kuchitsu, K. *J. Chem. Phys.* 1966, 44, 906.